MICROROBOTS

Acrobatics at the insect scale: A durable, precise, and agile micro–aerial robot

Suhan Kim[1]†, Yi-Hsuan Hsiao[1]†, Zhijian Ren[1], Jiashu Huang[1,2], Yufeng Chen[1]*

Aerial insects are exceptionally agile and precise owing to their small size and fast neuromotor control. They perform impressive acrobatic maneuvers when evading predators, recovering from wind gust, or landing on moving objects. Flapping-wing propulsion is advantageous for flight agility because it can generate large changes in instantaneous forces and torques. During flapping-wing flight, wings, hinges, and tendons of pterygote insects endure large deformation and high stress hundreds of times each second, highlighting the outstanding flexibility and fatigue resistance of biological structures and materials. In comparison, engineered materials and microscale structures in subgram micro–aerial vehicles (MAVs) exhibit substantially shorter lifespans. Consequently, most subgram MAVs are limited to hovering for less than 10 seconds or following simple trajectories at slow speeds. Here, we developed a 750-milligram flapping-wing MAV that demonstrated substantially improved lifespan, speed, accuracy, and agility. With transmission and hinge designs that reduced off-axis torsional stress and deformation, the robot achieved a 1000-second hovering flight, two orders of magnitude longer than existing subgram MAVs. This robot also performed complex flight trajectories with under 1-centimeter root mean square error and more than 30 centimeters per second average speed. With a lift-to-weight ratio of 2.2 and a maximum ascending speed of 100 centimeters per second, this robot demonstrated double body flips at a rotational rate exceeding that of the fastest aerial insects and larger MAVs. These results highlight insect-like flight endurance, precision, and agility in an at-scale MAV, opening opportunities for future research on sensing and power autonomy.

INTRODUCTION

Insect flight is characterized by fast body dynamics, complex flapping-wing kinematics, and unsteady aerodynamics. Fast neural reflexes and motor control enable aerial insects to quickly evade predators (*1*) and recover attitude stability (*2*). When aerial insects execute banked turns (*3*), body saccades (*4*), or inverted landing (*5*), they experience large rotational speeds (>2000° s^{-1}) far exceeding those of birds and micro–aerial vehicles (MAVs). Aerial insects are also precise flyers when they hover around a flower's anther amid a gentle breeze. This exceptional agility and precision are enabled by flapping-wing propulsion that can generate large instantaneous forces and torques. During flight, the insect wing hinge converts the power muscle oscillation into a back-and-forth wing motion ranging from tens to hundreds of times per second. This biomechanical structure is sophisticated and durable. It exerts precise control of wing kinematics through many steering muscles and endures large tensile and compressive stress induced by aerodynamic loading and muscle actuation. For instance, the *Drosophila* wing hinge connects to 12 steering muscles (*6*), and it can control the wing beat motion along all three rotational axes with a fine resolution of less than 2°. When a fly encounters a large disturbance, evades predators, or suffers wing damage (*7*), the flapping frequency and amplitude are adjusted over large ranges of 50 Hz and 30°, respectively. Under these harsh mechanical conditions, the hinge can operate millions of wing beat cycles, critical to the survival and functioning of aerial insects.

Inspired by tiny natural flyers, researchers have developed numerous biomimetic MAVs (*8*–*12*) with the goal of achieving insect-like flight capabilities. Mesoscale (10 to 30 g) flapping-wing robots (*8*, *9*, *13*, *14*) have demonstrated stable hovering flight and biomimicking maneuvers such as saccade and body flips. However, owing to their larger sizes and weights, these robots have slower body dynamics. Their wing beat frequencies and maximum body angular velocities are substantially slower than those of aerial insects. To miniaturize robot size, electromagnetic motors must be replaced by low-friction and power-dense microscale actuators. Piezoelectric bimorph actuators (*15*) exhibit high bandwidth and force density, and they lead to a class of subgram MAVs (*10*, *16*–*18*). These robots have achieved hovering flight (*10*), trajectory tracking (*16*), and biomimetic demonstrations such as perching (*19*) and hybrid aerial-aquatic locomotion (*20*). Recently, power-dense dielectric elastomer actuators (DEAs) were developed and applied in subgram MAVs (*21*). The soft actuators exhibited muscle-like robustness and resilience, enabling damage resilience (*22*) and collaborative payload transport (*23*). These advances highlight the unique flight capabilities of subgram MAVs in comparison with mesoscale aerial robots.

However, the flight performance of aerial insects remains far superior to that of subgram MAVs. Aside from relying on off-board power and control, subgram MAVs have limited flight endurance, speed, accuracy, and agility. This performance gap is largely attributed to the lack of fabrication methods and engineered materials for building similar biomechanical structures in insects. Although the smart composite manufacturing (SCM) (*24*) method can fabricate three-dimensional (3D) structures with micrometer-level resolution, it remains difficult to incorporate compatible materials that exhibit high flexibility and durability. For example, the elastomeric protein resilin is a durable, elastic, and low-loss material found in the insect wing hinge ligament. It can be stretched up to three times its nominal length and shows a fatigue limit of 300 million cycles (*25*). In contrast, biomimetic flexures in MAVs are built with thin-film polyimide, which has an elongation ratio and fatigue limit of merely 0.72 and 300,000 cycles, respectively. Under a similar geometry, the transmission and hinge in subgram MAVs exhibit

[1]Department of Electrical Engineering and Computer Science, Massachusetts Institute of Technology, 77 Massachusetts Avenue, Cambridge, MA 02139, USA. [2]Department of Physics, Brown University, 69 Brown Street, Providence, RI 02912, USA.
*Corresponding author. Email: yufengc@mit.edu
†These authors contributed equally to this work.

substantially shorter lifespans. Owing to this materials challenge, most existing subgram MAVs (*26*) are limited to short flights of within 10 s, and they require frequent tuning and repair. The lack of flight endurance also constrains other flight capabilities. Given a short lifespan, it becomes difficult to accurately estimate the robot's inertial parameters, measure force and torque mappings, and develop well-tuned controllers. Most subgram MAVs (*10*, *16*, *27*) are limited to performing hovering flights or following simple trajectories at a speed lower than 10 cm s^{-1}. In the rare example of performing a somersault (*28*), previously described robots could not recover attitude stability before rebounding on the floor, which is caused by inaccurate force and torque mappings under a limited number of characterization experiments. These limitations underscore the importance of developing a durable subgram MAV, which is critical to improve flight speed, accuracy, and agility.

In this work, we developed a 750-mg four-winged MAV (Movie 1 and Fig. 1, A and B) with substantially improved flight endurance, speed, accuracy, and agility. We identified off-axis loading as the main contributor to flexure fatigue and failure and then designed an airframe, a transmission, a hinge, and a wing (Fig. 1C) to minimize off-axis torsion. The robot demonstrated a 1000-s hovering flight, two orders of magnitude longer than most existing subgram MAVs. This long lifespan allows extensive robot characterization and leads to a flight controller that improves flight precision under dynamic conditions. The robot demonstrated a sequence of trajectory-tracking flights with subcentimeter accuracy and an average speed of 30 cm s^{-1}. As an example, Fig. 1D shows a composite image where the robot followed the letters "MIT," with a root mean square (RMS) position error of 0.73 cm. Furthermore, the robot design enabled acrobatic maneuvers through reducing the moment of inertia and increasing the body torque generation. With a lift-to-weight ratio of 2.2 and a maximum ascending speed of 100 cm s^{-1}, the robot achieved a double flip within 0.17 s. During this maneuver, the maximum body roll rate exceeded 7200° s^{-1}, which is 40% faster than fruit flies (*5*) and quadruples that of the fastest aerial robot (*29*). These flights showcase insect-level performance in a subgram MAV, and they also open opportunities for future research on sensing and power-autonomous microsystems.

Movie 1. Overview of robot design, static characterization, and flight experiments. A 750-mg flapping-wing robot demonstrates 1000-s hovering flight, precise tracking of complex trajectories, and acrobatic body flips.

RESULTS

Design of a long-endurance and agile flapping-wing robot

Compared with aerial insects, previously described subgram MAVs had limited flight time and agility. We designed a four-winged aerial robot (Fig. 1A) that demonstrated long flight endurance and acrobatic maneuvers. The 750-mg robot had four identical modules with a compact dimension of 4 cm by 4 cm by 0.9 cm (Fig. 1B). Each module consisted of an airframe, a DEA, a set of transmissions, and a wing with its long hinge (Fig. 1C).

The module was designed to maintain high structural consistency under the large stress and strain induced by the flapping-wing motion. The cylindrical DEA had a diameter and length of 5.8 and 5 mm, respectively. Compared with rigid actuators, DEAs have a lower modulus and are susceptible to off-axis deformation (*21*). The carbon fiber airframe (Fig. 1C and fig. S1A) consisted of six I-beams to minimize structure oscillations during DEA actuation. Three sets of a linear four-bar transmission connected the DEA to the airframe. In addition to converting the DEA's linear elongation to the wing rotational motion (*21*), the transmissions reduced the DEA off-axis deformation by constraining it along the longitudinal axis. The wing had a long hinge along its leading edge (Fig. 1C) to endure the stress and strain of flapping. Compared with the shorter wing hinges in prior works (*21*, *30*), this design reduced the hinge stress by more than 1000 times, leading to a substantial increase in the hinge lifespan.

This modular design also enabled precise and agile flight maneuvers by reducing robot moment of inertia and increasing flight torque generation. Compared with rotary designs where the motor and the propeller were placed along the same axis, flapping-wing designs offset the wing from the actuator. In our robot, the distances from the robot center of mass (COM) to each module's COM and center of pressure (COP) were 8.7 and 22.5 mm, respectively (Fig. 1C). The robot had small moments of inertia owing to the small distance between the robot COM and each module's COM, yet it could generate large body torques because of the large robot COM-to-COP distance. Consequently, this design allowed the robot to generate large angular acceleration under small changes in lift forces, which enabled aggressive control and fast maneuvers. The main robot design parameters included the transmission ratio, wing size, and hinge stiffness. A detailed description of parameter selection is given in the "Selection of robot design parameters" section in Supplementary Methods and fig. S2.

Static characterization of robot performance

We conducted a series of statically constrained experiments (Fig. 2, A to C, and fig. S2, A to C) to evaluate robot performance. Figure 2A and movie S1 part 1 show a static flapping-wing experiment where the DEA operated at 1925 V and 330 Hz. Like prior designs (*21*), the flapping-wing motion had two degrees of freedom: the wing stroke and pitch motion. The DEA oscillation directly drove the wing stroke motion, whereas the wing pitch motion was passive. The instantaneous wing stroke and pitch angles are shown in Fig. 2D, and their peak-to-peak amplitudes were 41° and 118°, respectively. Compared with that of prior designs, the stroke amplitude became substantially smaller to reduce flexural strain in the four-bar transmission. This reduction in the stroke amplitude was compensated by a two-times increase in the wing area, which generated sufficient lift forces for enabling flight. To measure the net lift force, we mounted the robot on a beam that was balanced around a pivot. We operated the robot

at the same conditions of 1925 V and 330 Hz and filmed its liftoff process (Fig. 2B and movie S1 part 2). The robot ascended 5.2 cm in 0.6 s while carrying a 360-mg payload inclusive of its weight. Through tracking the robot liftoff angle and fitting to a dynamical model (*28*), we measured the net lift force to be 4.0 mN, equivalent to a lift-to-weight ratio of 2.2.

To characterize robot performance across different operating conditions, we varied the driving voltage and frequency in static flapping and liftoff experiments. Figure 2E shows flapping experiments where voltage and frequency were set independently in the ranges of 1300 to 1925 V and 100 to 500 Hz, respectively. The wing stroke amplitude reached a maximum near 300 Hz, which implied that the net lift force also maximized around a similar frequency. Next, we repeated liftoff tests (Fig. 2B and movie S2 part 2) under different driving conditions. Figure 2F showed the measured lift force as functions of driving voltage and frequency, and it reached a maximum at the 330-Hz condition. On the basis of this result, we fixed the operating frequency to 330 Hz for all flight experiments. The red curve in Fig. 2F represents the voltage-to-lift force mapping applied in the flight controller. Similar to prior works (*28*, *30*), we modeled the DEA as a series resistor-capacitor (RC) element and found the equivalent R and C to be 78 kilohms and 1.48 nF, respectively. The 330-Hz operating condition was close to the mechanical resonance frequency determined by the wing-transmission-actuator system given that the RC time constant indicated that the electrical resonance frequency was more than 1 kHz. Using a custom circuit, we measured the robot power consumption during liftoff flight and obtained a lift-to-power ratio of 9.4 mN W^{-1}. The robot efficiency was similar to our prior works (*28*, *30*) but approximately five times worse than piezoelectric flyers (*10*).

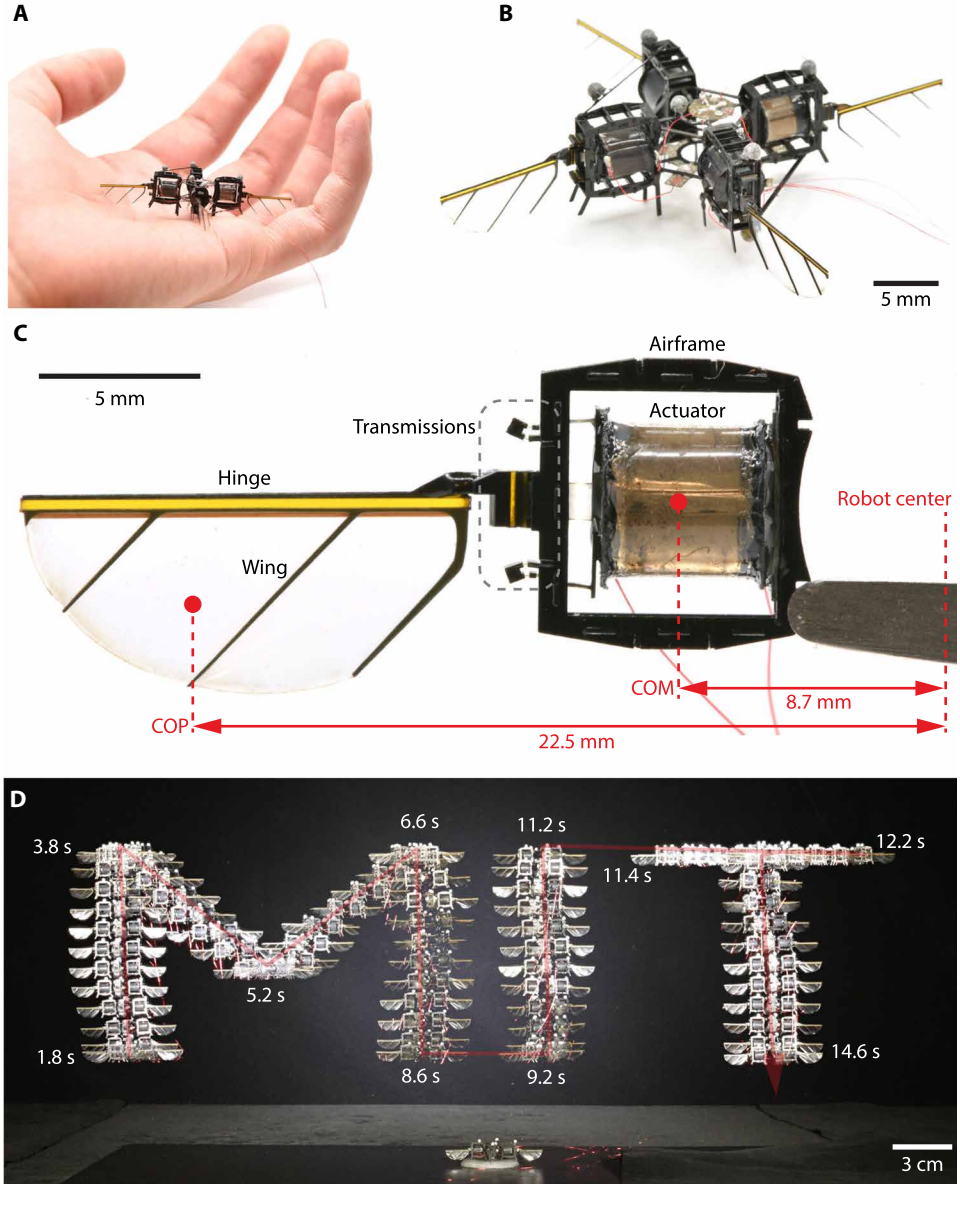

Fig. 1. A long-endurance, precise, and agile insect-scale flapping-wing robot. (**A**) An image of the robot resting on a human palm. (**B**) This 4 cm–by–4 cm–by–0.9 cm robot consisted of four identical modules. (**C**) Each robot module had a soft actuator, an airframe, a set of transmissions, and a wing with a long hinge. (**D**) A composite image of a trajectory-tracking flight in which the robot traced the letters MIT. Scale bar, 3 cm.

Next, we characterized robot torque generation by mounting it around a fixed post and measuring its rotational speed (Fig. 2C). When the robot was driven at 1800 V and 330 Hz, it revolved around the post four times in 0.205 s (Fig. 2C and movie S1 part 3). By tracking the instantaneous rotation angle (fig. S2I), we measured an average angular acceleration of 46,200° s^{-2}. The maximum angular speed reached 9700° s^{-1}, which implied that the robot could generate a large body torque and perform aggressive maneuvers.

In addition to quantifying robot force and torque production, we demonstrated substantial improvement in robot actuation consistency and lifespan. The prior wing hinge design (Fig. 3A) mimicked the relative dimension of an insect wing hinge (*6*), which was less than 20% of the wingspan. Although resilin protein in the insect hinge could endure large cyclic loading and deformation, the polyimide flexure in the robot hinge had a far shorter fatigue limit. We conducted a numerical simulation where a static load was applied at the wing's COP. The static loading force was set to 5 mN, equivalent to the estimated drag force during hovering flight (*31*). The insets in Fig. 3A show that stress was concentrated near the hinge's lower left and upper right corners, which suggested that cracks might initiate along these high-stress regions.

To verify this simulation result, we conducted static flapping-wing experiments with the wing hinge pair in Fig. 3A. We drove the wing at the robot liftoff condition until we observed sudden hinge failure (Fig. 3, B and C, and movie S2 part 1). In this experiment, the flapping-wing motion became anomalous after ~200 s, and then a crack quickly developed and

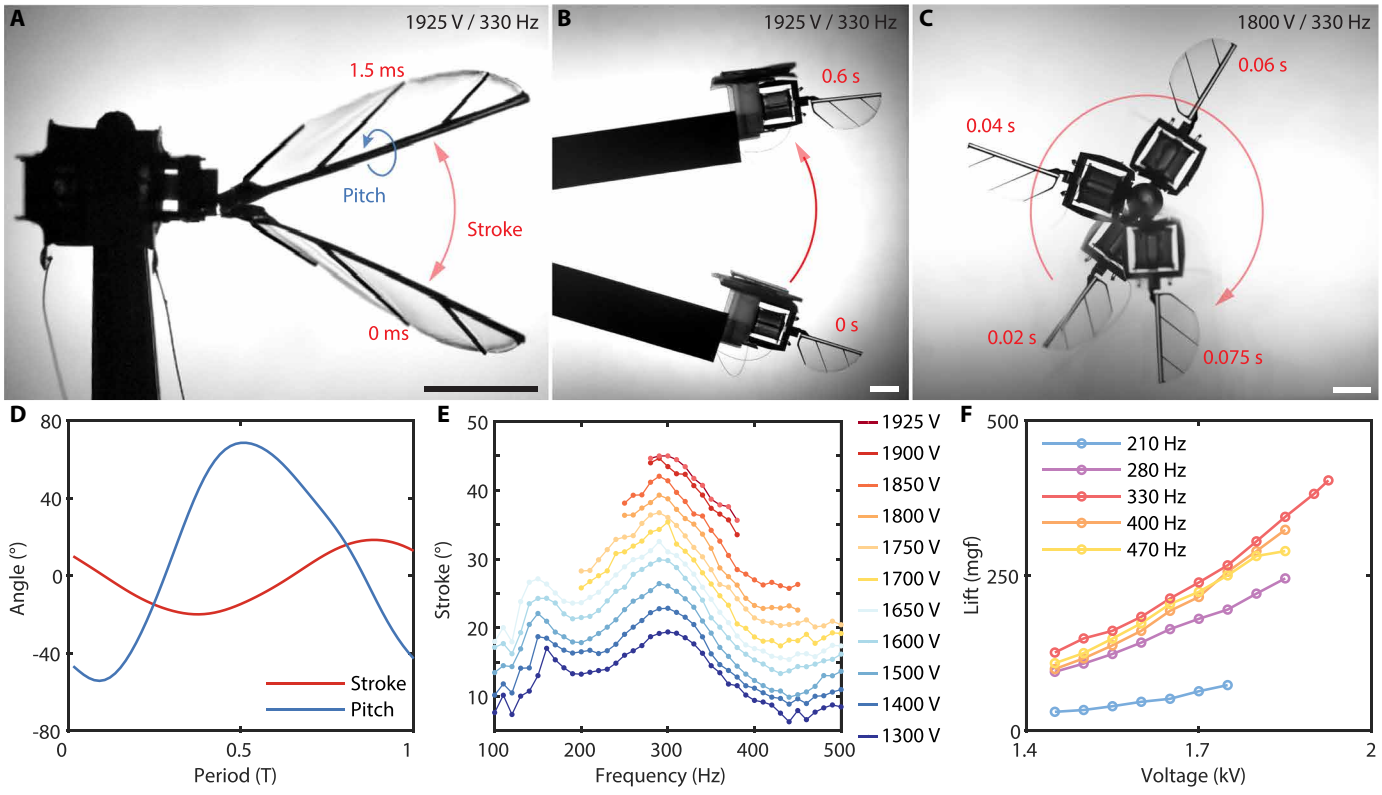

Fig. 2. Static characterization of robot performance. (**A**) A composite image of the robot flapping-wing motion when it was operating at 1925 V and 330 Hz. (**B**) A composite image of robot liftoff when it carried a 180-mg payload. The robot achieved a maximum lift-to-weight ratio of 2.2. (**C**) A composite image of the robot rotation experiment. (**D**) Measured instantaneous wing stroke and pitch motion that correspond to (A). (**E**) Robot stroke amplitude as functions of operating voltage and frequency in flapping experiments. (**F**) Robot lift force as functions of driving voltage and frequency in liftoff experiments. Each dot in (E) and (F) corresponds to a separate experiment where the driving frequency and voltage were set independently. The scale bars in (A) to (C) represent 5 mm.

propagated through the entire hinge. Figure 3B shows an image of the torn hinge that failed within four wingbeats (Fig. 3C). This sudden hinge failure immediately led to a loss of lift force, further destabilizing flight (movie S2 part 2). This hinge fatigue problem was exacerbated as the wing size increased. Under the same wing hinge, we found that the hinge lifespan decreased by 10 times when the wing area was scaled up by two times (fig. S1F).

To address this problem, we redesigned the wing hinge to reduce flexural stress. In this design, the polyimide flexure extended through the entire wing (Fig. 3D). In comparison, the distance from the wing COP to the hinge center was reduced from 5.5 (Fig. 3A) to 0.7 mm (Fig. 3D). A numerical simulation showed that the maximum hinge stress decreased by more than 1000 times. After this simulation result, we conducted static flapping and flight experiments to measure the hinge lifespan. After enduring more than 1000 s of static flapping and 1500 s of flight experiments, the wing and hinge did not exhibit any degradation or failure. This was an important result because the robot no longer suffered sudden wing loss during flight.

Our robot design also mitigated performance degradation due to off-axis actuator bending. The DEAs are muscle-like soft actuators that elongate along the axial direction. However, a large axial load due to aerodynamic forces may lead to dynamic buckling (*21*) along the off-axis direction. In the original design, the linear four-bar transmission was compliant in the off-axis direction (Fig. 3E). When the robot operated near peak performance conditions, the DEA deformed laterally (Fig. 3E and movie S3), which reduced the wing stroke amplitude and the associated lift force. This off-axis DEA bending may also lead to electrical shorting and degrade DEA performance.

To mitigate this problem, we added two guide transmissions that constrained DEA off-axis bending (Fig. 3F). Figure 3F and movie S3 show that the robot was operated at the same conditions of 1850 V and 330 Hz. Compared with the old design (red curve in Fig. 3G), this design showed a 78% decrease in off-axis displacement and an 87% increase in axial elongation. This translated to a greater than 80% increase in wing stroke amplitude, suggesting a large increase in lift force production. This addition of guide transmissions increased the robot lift force at peak operating conditions, reduced transmission deformation, and improved robot endurance. In addition, the robot actuator, transmission, and hinges consisted of compliant materials that exhibit collision resilience. While the robot was operating at 1800 V and 330 Hz, we hit the robot wing with a stick (Fig. 3H and movie S1 part 4), which reduced the wing stroke motion. After the stick was removed, the robot flapping-wing motion recovered to the nominal amplitude within four wingbeats (Fig. 3, H and I), indicating that the robot was robust against collisions.

With this robot design, we performed constrained liftoff experiments (Fig. 2B) to quantify DEA degradation. The robot was mounted on the liftoff stand and was driven at 330 Hz and a minimum liftoff voltage for 10 s. If the robot could lift off, then we repeated the experiment at the same operating conditions. If

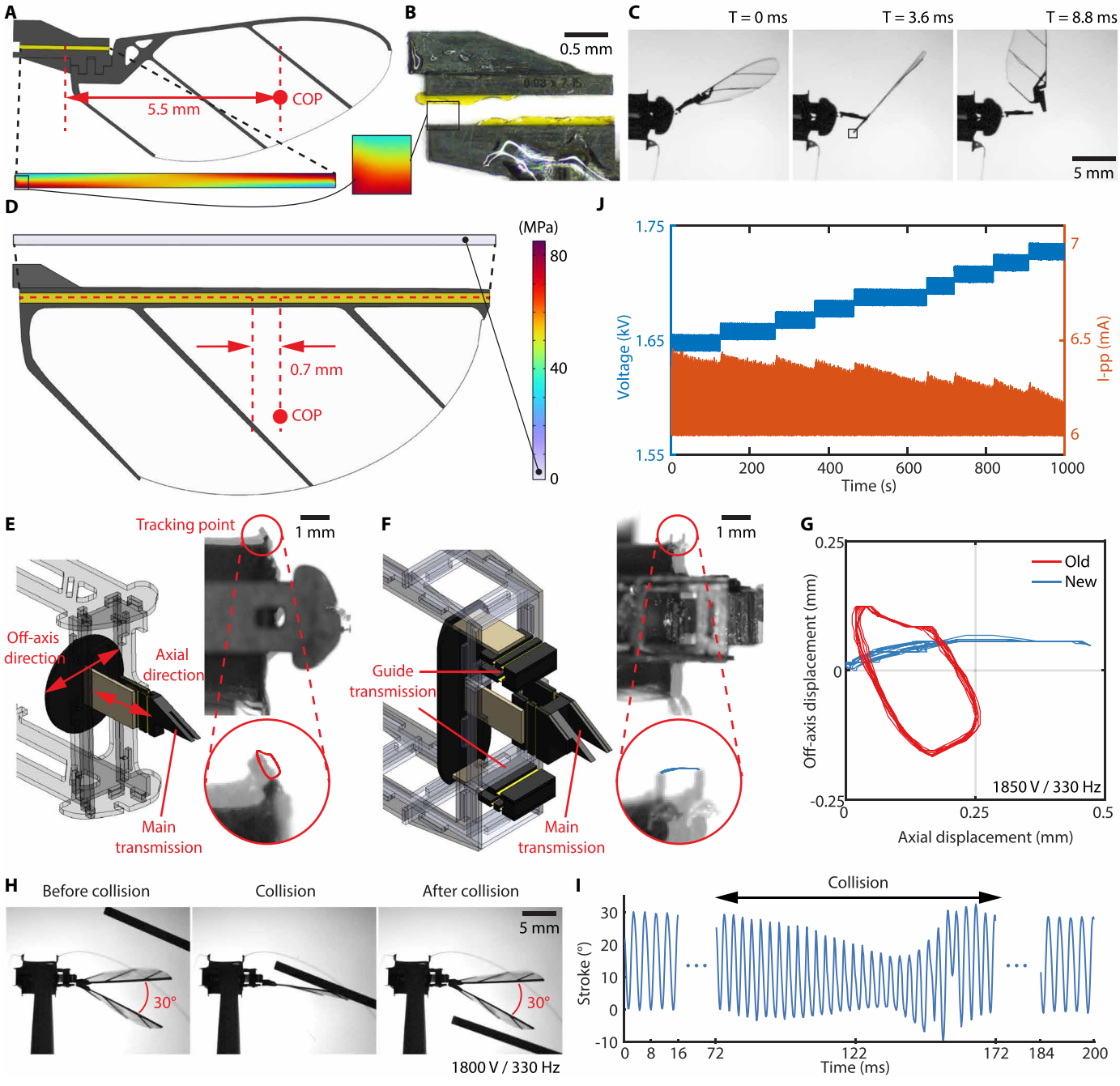

Fig. 3. Experimental characterization of wing hinge and transmission performance. (**A**) An illustration of the prior wing and hinge design. The inset shows a finite element COMSOL simulation of hinge stress when the robot was operating at the hovering condition. High stress concentrated near the hinge root and tip. (**B**) An image of the torn hinge. Scale bar, 0.5 mm. (**C**) An image sequence that showed sudden wing hinge failure. Scale bar, 5 mm. (**D**) An illustration of the wing and hinge design in this work. The inset shows a COMSOL simulation of hinge stress under the same operating condition as in (A). The stress concentration plots in (A) and (D) share the color scale, which showed the maximum stress in (D) reduced by more than 1000 times. (**E**) A prior design of the linear four-bar transmission. The overlaid image shows large actuation hysteresis. Scale bar, 1 mm. (**F**) A transmission design that constrained off-axis motion. The overlaid image shows that DEA actuation is mostly axial. Scale bar, 1 mm. (**G**) Comparison of DEA deformation under different transmission designs in (E) and (F). (**H**) The robot wing was hit by a stick while it was operating at 330 Hz with 30° stroke amplitude. The flapping-wing motion recovered to nominal amplitude after the stick was removed. Scale bar, 5 mm. (**I**) The measured wing stroke motion before, during, and after collisions. (**J**) Commanded voltage amplitude and measured current during a 1000-s static liftoff experiment.

the robot could not lift off, then we increased the driving voltage by 10 V. We repeated the experiments until the robot completed 1000 s of cumulative liftoff flight. Figure 3J shows the commanded voltage (blue) and the measured current (red). Over the 1000-s operation, the minimum liftoff voltage increased by 4.8% and the current decreased by 4%. These data showed the robot's potential to operate for an extended duration far exceeding tens of seconds.

Long-endurance hovering flight

We conducted a sequence of hovering flights to evaluate robot endurance. In our flight experiments, the robot was tethered to offboard power sources (Trek 2220) and relied on an external motion capture system (Vicon Vantage V5). We designed a feedback flight controller that received tracking data at 400 Hz and commanded the robot at 2 kHz. Compared with prior work (*21*), this controller introduced three features for reducing positional error during dynamic maneuvers. The controller implementation details are described in the "Flight controller design" section of Supplementary Methods.

To assess robot consistency and lifespan, we gradually increased the flight time from 10 to 60, 100, 400, and 1000 s. The shorter flights are described in the "Robot flight repeatability" section of Supplementary Methods and in fig. S3. Figure 4A shows a composite image sequence of the 1000-s flight (movie S4) where the robot hovered 7 cm above the ground. The RMS errors of the lateral position (Fig. 4B) and altitude (Fig. 4C) were 2.35 and 0.14 cm, respectively. Compared with most prior results (*21*, *28*, *30*), the flight time increased by 100 times while the robot maintained a similar flight accuracy. During this flight, the robot slowly drifted along the positive x and negative y directions (Fig. 4B), which was contributed by gradual DEA heating and degradation. Figure 4D shows the driving voltage amplitude of the four actuators. Over this 1000-s flight, the commanded voltage of the first DEA (dark green curve in Fig. 4D) increased from 1720 to 1850 V, representing a 7.56% deviation from the calibrated controller values. This performance degradation was likely contributed by self-clearing during flight, and the DEA did not recover to a nominal performance after cooling down to room temperature. The lateral position error could be further reduced under an adaptive flight controller that accounted for the changing performance.

Overall, this 1000-s flight represented orders-of-magnitude improvement in hovering time among subgram MAVs. Before requiring actuator replacements, the robot performed consecutive long flights where the total hovering time exceeded 1550 s. Unlike prior designs (movie S2 part 2), this robot never experienced sudden hinge or actuator failure that could destabilize the flight. This high consistency and long lifespan enabled follow-up experiments on complex trajectory tracking and aggressive acrobatics.

Fast and precise trajectory tracking flights

In addition to achieving long endurance flights, we performed a sequence of trajectory tracking demonstrations that highlighted robot precision and speed. First, our robot tracked a 20 cm-by-10 cm "∞" (infinity sign) similar to that of a recent work (*16*). While performing this flight (Fig. 5A and movie S5), the robot closely followed the desired x and z trajectories (Fig. 5, B and C) with lateral and altitude errors of 0.97 and 0.29 cm, respectively. The average flight speed reached 31.4 cm s^{-1} (Fig. 5D) while the robot tracked the infinity sign. Compared with a recent work (*16*), our robot tracked the same trajectory with a speed that was 3.1 times faster, yet the position and altitude errors were reduced by 61.8 and 42%, respectively. This benchmark flight showed the highest flight precision and speed among subgram aerial robots. To demonstrate robot consistency, we repeated the same flight five times (fig. S4).

Next, our robot tracked two nested circles that were 10 cm above the xy plane (Fig. 5E and movie S6). The outer circle had a dimension of 12 cm by 12 cm, and the robot followed it with a speed of 36 cm s^{-1} and a positional error of 0.91 cm for the entire flight. Compared with a prior work that tracked a similar trajectory (*32*), our robot demonstrated a five times reduction in the RMS position error (Fig. 5, F and G) at an eight times higher flight speed (Fig. 5H). This

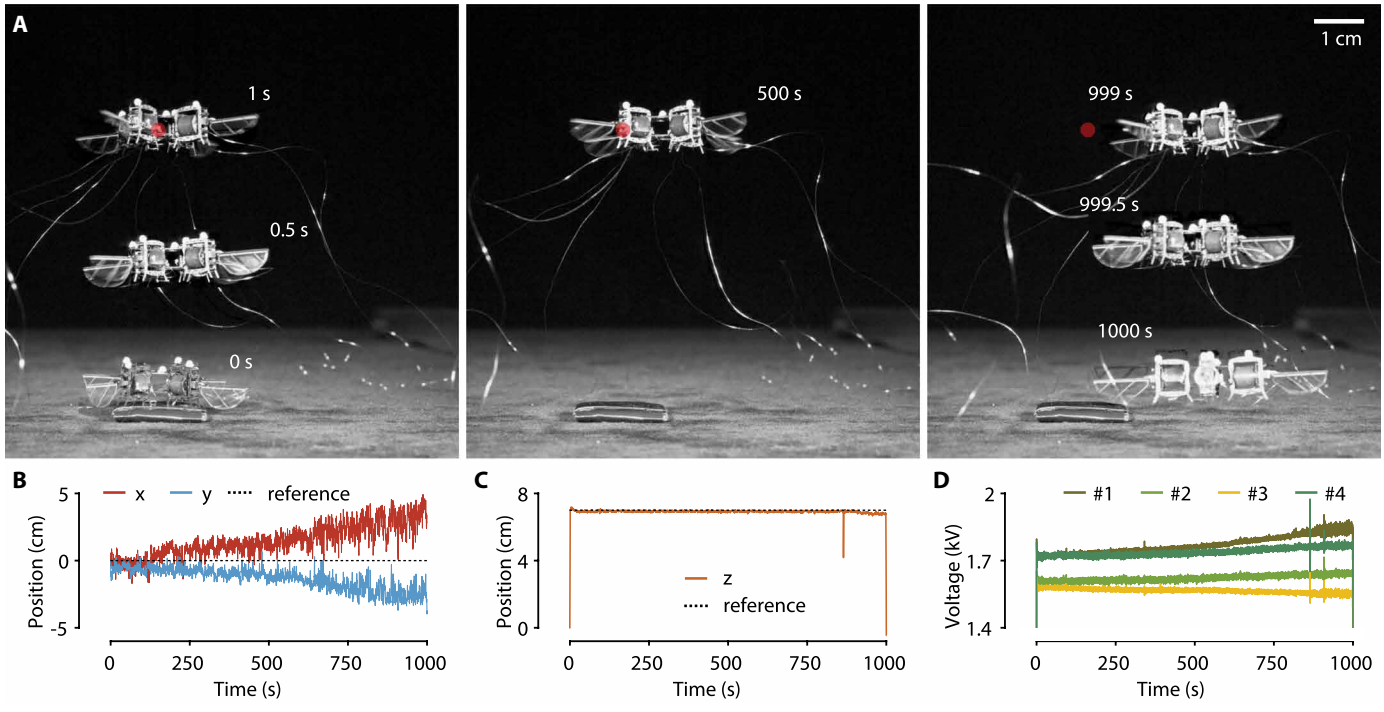

Fig. 4. A 1000-s, long-endurance hovering flight. (**A**) A composite image sequence showing the 1000-s hovering flight. Scale bar, 1 mm. (**B** and **C**) Tracked robot lateral position (B) and altitude (C) during the flight. (**D**) Commanded voltage amplitudes sent to the four independent actuators.

flight was repeated five times (fig. S5) to highlight robot and controller consistency.

In addition to tracking simple trajectories (Fig. 5, A to H), our robot can follow complex paths that are difficult for other subgram robots. We designed a 20 cm–by–20 cm–by–10 cm 3D trajectory where an infinity sign gradually rotated along the *z* axis (Fig. 5I and movie S7). The robot tracked the rotating pattern 15 times during a 34-s flight. Figure 5 (J and K) shows that the measured *x*, *y*, and *z* positions closely follow the desired path. The robot maintained a mean speed of 30 cm s^{-1} (Fig. 5K) while it tracked this 9.7-m-long trajectory, the longest flight path flown by a subgram MAV. The RMS lateral position and altitude errors of this flight were 1.05 and 0.34 cm, respectively. This flight was repeated five times (fig. S6).

Our robot achieved smaller position and altitude errors when it flew at a slower speed. To demonstrate high flight precision, we commanded the robot to trace the letters "MIT" (Fig. 1E and movie S8) at a slower speed of 7.48 cm s^{-1}. This trajectory had a dimension of 46 cm by 12 cm, and it was challenging because of frequent stopping and changing of flight directions. Figure S7 shows the six flights our robot performed, with mean RMS lateral position and altitude errors of 0.80 and 0.20 cm, respectively. Compared with the 3D trajectory in Fig. 5I, the position and altitude errors were reduced by 24 and 41%, respectively. The lateral position and altitude errors of all four trajectory-following flights are compared in Fig. 5 (L and M), which show that the flight precision improves when the flight speed decreases. The 3D infinity– and letter-following flights represented

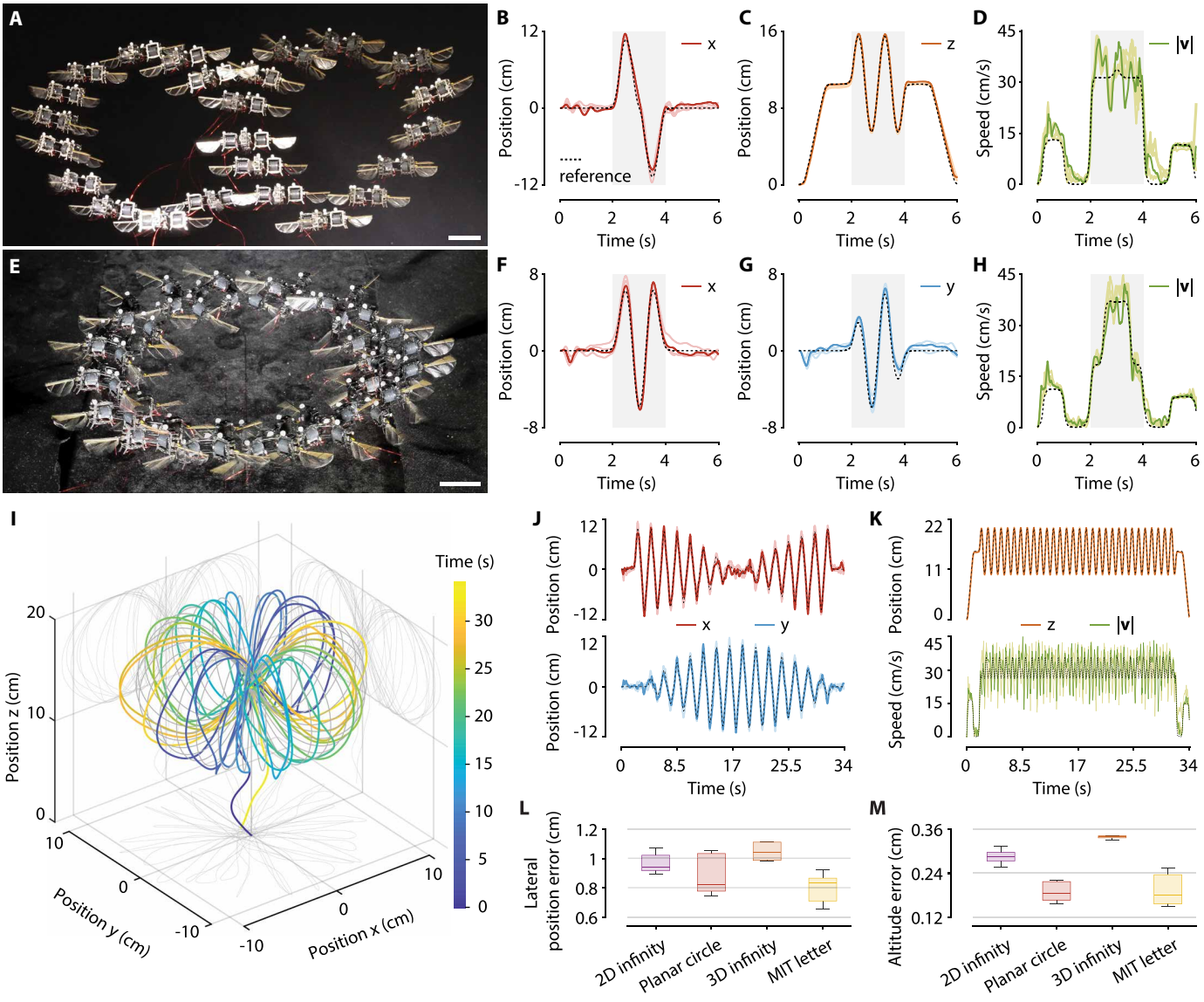

Fig. 5. Trajectory-following demonstrations. (**A**) A composite image of the robot following an infinity sign. (**B** to **D**) Robot *x* (B) and *z* (C) positions and flight speed (D) that correspond to the flight in (A). (**E**) A composite image of the robot tracking a planar circle. (**F** to **H**) Robot *x* (F) and *y* (G) positions and flight speed (H) that correspond to the flight in (E). (**I**) The tracked trajectory when the robot followed a rotating infinity pattern. (**J** and **K**) Robot *x*, *y*, and *z* positions and the flight speed that correspond to the flight in (I). The trajectory-following flights in (A), (E), and (I) were repeated five times. The darker colored curves in (B) to (D), (F) to (H), and (J) and (K) correspond to the flights in (A), (E), and (I), respectively. The lighter colored curves represent the repeating flights. (**L** and **M**) RMS lateral (L) and altitude (M) errors of the four trajectories. Colored boxes show 25, 50, and 75 percentiles, and the black bars show minimum and maximum errors. The scale bars in (A) and (E) represent 1 cm.

some of the longest and most complex paths flown by subgram MAVs. These demonstrations were enabled by the robot's high consistency and its ability to generate large body torques. The trajectory design is described in the "Flight trajectory design" section of Supplementary Methods.

Demonstrations of acrobatic flight maneuvers

In addition to performing fast and precise flights, our robot demonstrated insect-like acrobatic maneuvers (movies S9 and S10). Figure 6 (A to C) shows a composite image sequence of a somersault demonstration. The robot took off and hovered around a set point for 1 s (Fig. 6A). Next, it accelerated upward until the ascending speed exceeded 80 cm s^{-1}. Then, it performed the somersault within 0.11 s (Fig. 6B) and recovered attitude stability (Fig. 6C). Last, the robot returned to the hovering set point and landed (Fig. 6C). Figure 6 (D to F) shows the tracked robot position, altitude, attitude, flight velocity, and angular velocity. This flight was repeated five times (fig. S9) to demonstrate robot consistency. The controller design is described in the "Controller design for executing body flips" section of Supplementary Methods and in fig. S8.

This flight showed a complete body flip performed by a subgram MAV. In a prior work (*28*), another subgram MAV demonstrated a body flip, but it could not recover altitude before hitting the ground. In comparison, our robot could recover attitude stability without dropping height (Fig. 6E). The robot completed the somersault within 0.11 s. During this maneuver, the maximum robot angular velocity exceeded 4800° s^{-1}.

Our robot could further perform double body flips, a challenging maneuver that has never been achieved by flapping-wing robots across scales. Figure 6 (G to I) shows a composite image sequence of this flight. Similar to the single body flip, the robot took off, hovered, ascended, flipped twice, recovered stability, and finally landed. The measured robot position, velocity, attitude, and angular velocity are shown in Fig. 6 (J to L). In this flight, the robot completed two body flips within 0.17 s. When the robot accelerated upward, its maximum ascending speed exceeded 100 cm s^{-1}. During the flipping process, the robot's maximum angular velocity reached 7200° s^{-1} (Fig. 6L). After the robot recovered its attitude stability, it only lost 6.22 cm of height (Fig. 6K) compared with the start of the flip. These flight performances exceeded those of existing subgram MAVs and were comparable to those of aerial insects (*5*). This acrobatic flight was repeated five times (fig. S10) to demonstrate robot consistency under aggressive operating conditions.

DISCUSSION

In this work, we developed a soft-actuated MAV that exhibits long endurance, high flight precision, and insect-like agility. These flight capabilities were enabled by mechanism, configuration, and controller designs that address prior challenges. Stress-relieving transmissions and hinges substantially improved the hardware consistency; the four-wing configuration enhanced lift force generation by avoiding adverse wing-wing interactions that relate to the inward facing wing pairs in prior eight-wing designs (*21*). These hardware designs resulted in substantial improvements in flight endurance and maximum ascending speed. In the past, subgram MAVs were limited to flying for less than 20 s at low speeds (blue dots in Fig. 7A). Our robot showed a 1000-s hovering flight, almost two orders of magnitude longer than most subgram MAVs, and its ascending speed exceeded 100 cm s^{-1}, which is twice that of similar-sized rigid-driven MAVs. In addition to hardware advances, we designed a controller for improving flight precision, which could be quantified by measuring the position error of hovering or trajectory-following flights. The position error usually increases in faster and longer flights because of unaccounted aerodynamic effects and hardware drifting. In the past, subgram MAVs were limited to slowly (<15 cm s^{-1}) following short (<20 s) trajectories, and their position error ranged from 1.2 to 4.5 cm (blue dots in Fig. 7B). Our robot demonstrated much faster (>30 cm s^{-1}) trajectory-tracking flights with smaller position errors (red dots in Fig. 7B). The error in most flights was smaller than 1.4 cm (Fig. 7B), and it grew to 2.3 cm in the 1000-s hover because of slow DEA degradation. Our flight trajectories were also more challenging because they had frequent turns and longer pathlengths (Fig. 5). Overall, our robot and controller design achieved substantial improvements in flight endurance, speed, and precision (Fig. 7, A and B).

Furthermore, high hardware consistency and precise flight control enabled insect-like agility. Our robot demonstrated double body flips, a challenging acrobatic maneuver for flapping-wing robots across scales. This performance was competitive against rotary MAVs and natural flyers (Fig. 7C). Inertial scaling predicts that the robot's rotational speed is inversely proportional to the wing or rotor size, suggesting that smaller robots can perform somersaults at a faster rate. This trend is supported by Fig. 7C, which shows that our robot achieves the fastest rotation compared with other drones (blue) in the plot. In addition, our robot is also faster than the blue bottle fly, a fast flipping aerial insect (*5*).

These flight demonstrations have implications for the microrobotics and the soft robotics communities. Achieving insect-like endurance, precision, and agility opens opportunities for emulating complex insect functions. It will inspire the subgram MAV community to move from hovering or simple trajectory-following demonstrations to accomplishing complex and extended tasks such as pollination and coordinated swarm flights. From the perspective of the soft robotics community, this work demonstrates controllability and agility comparable to that of rigid-driven systems. In the past, robustness and safety were salient features of soft actuators and mechanisms (*33*), but soft robotic systems fell behind in bandwidth and agility. Compared with existing soft robots, this tiny robot achieves some of the fastest speeds and turning rates without requiring normalization by its body length. It demonstrates that soft-driven robots can simultaneously embody robustness and agility. During the body flip maneuver, the DEAs respond to aggressive driving signals within milliseconds while they endure high stress and strain. These muscle-like properties outperform rigid actuators such as piezoelectric ceramics and microscale motors. This work will inspire future development of high-power soft actuators (*34*) and their applications in agile animal-like systems.

The substantial improvements in endurance, precision, and agility (Fig. 7, A to C) were enabled by robot designs that carefully considered the similarities and differences between biological and engineered systems. Our goal is to achieve insect-like flight performance in insect-scale robots, and it requires both biomimicking designs and engineered solutions. At this scale, rotary propulsion becomes infeasible because of a lack of efficient microscale motors. We chose the flapping-wing design and developed robust and muscle-like DEAs. These soft actuators have high resonance frequencies of 300 to 500 Hz, which implies that the robot can generate large

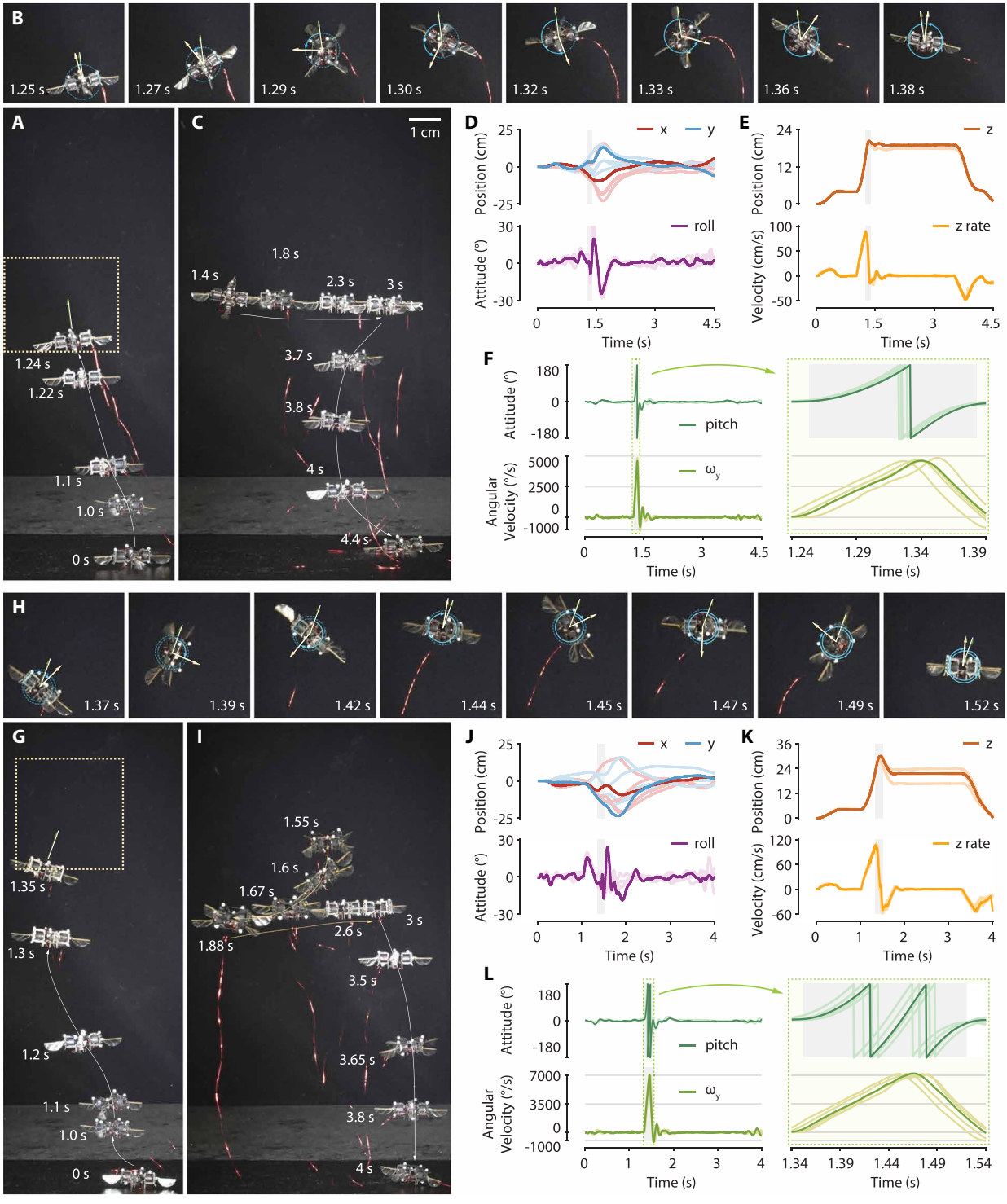

Fig. 6. Acrobatic flight demonstrations. (**A** to **C**) The robot performed a single body flip including ascent (A), body flip (B), recovery (C), and landing. (**D**) Tracked robot lateral position and roll angle. (**E**) Tracked robot altitude and ascending speed. (**F**) Robot pitch angle and angular speed. (D) to (F) correspond to the flights in (A) to (C). (**G** to **I**) The robot performed double body flips including ascent (G), consecutive body flips (H), recovery, and landing (I). (**J** to **L**) Tracked robot lateral position and roll angle (J), altitude and ascending speed (K), and pitch angle and angular velocity (L). (J) to (L) correspond to the flights in (G) to (I). The single and double flips were repeated five times. In (D) to (F) and (J) to (L), the darker colored curves represent the flight data in (A) to (C) and (G) to (I). The lighter colored curves are the repeating flights. The scale bar in (C) applies to (A) to (C) and (G) to (I). In (A) and (G), the rectangular regions represent the same cropped regions in (B) and (H) where the robot performed the flips. In (B) and (H), the green and yellow arrows indicate the start and instantaneous robot orientations, respectively.

instantaneous changes in forces and torques. In addition, flapping-wing MAVs are tolerant to collisions because of the reciprocal wing motion and the robot's low inertia. The use of artificial muscles and flapping-wing propulsion represents suitable biomimicking designs for achieving biomimetic functions.

However, under material and actuation constraints, it is also critical to adopt engineered designs that deviate from those in biological systems. For instance, insect hinges consist of resilin protein that exhibits a high fatigue limit under large cyclic loading and strain. In contrast, polyimide has a four times lower elongation ratio and 1000 times lower fatigue limit. Under a similar geometry, the robot hinge and transmission would experience failure (Fig. 3B) within 200 s. Our design reduced the hinge flexural stress by 1000 times by elongating the hinge width. It also reduced the transmission strain by decreasing the flapping-wing amplitude and maintained similar lift force by proportionally increasing the wing area. This wing hinge and transmission design principle can also benefit other subgram MAV platforms. Piezoelectric-driven MAVs (*10*, *16*, *19*) have a limited lifetime because of actuator cracking, which is caused by resonance mismatch when the flexures gradually soften. An elongated wing hinge and the proposed guide transmission designs can mitigate flexural degradation and contribute to longer endurance. Another design choice that deviates from biology is the use of four independently controlled wings. Insects have delicate muscle groups that exert fine control of the flapping-wing motion, but it is difficult to develop differently sized actuators and delicate transmissions for achieving three-degrees-of-freedom control of wing kinematics. We used four sets of actuators and wings to generate roll and pitch torques, which allowed the robot to achieve insect-like agile maneuvers and precision. This work demonstrates challenging bioinspired locomotive capabilities by combining biomimicking and engineered designs.

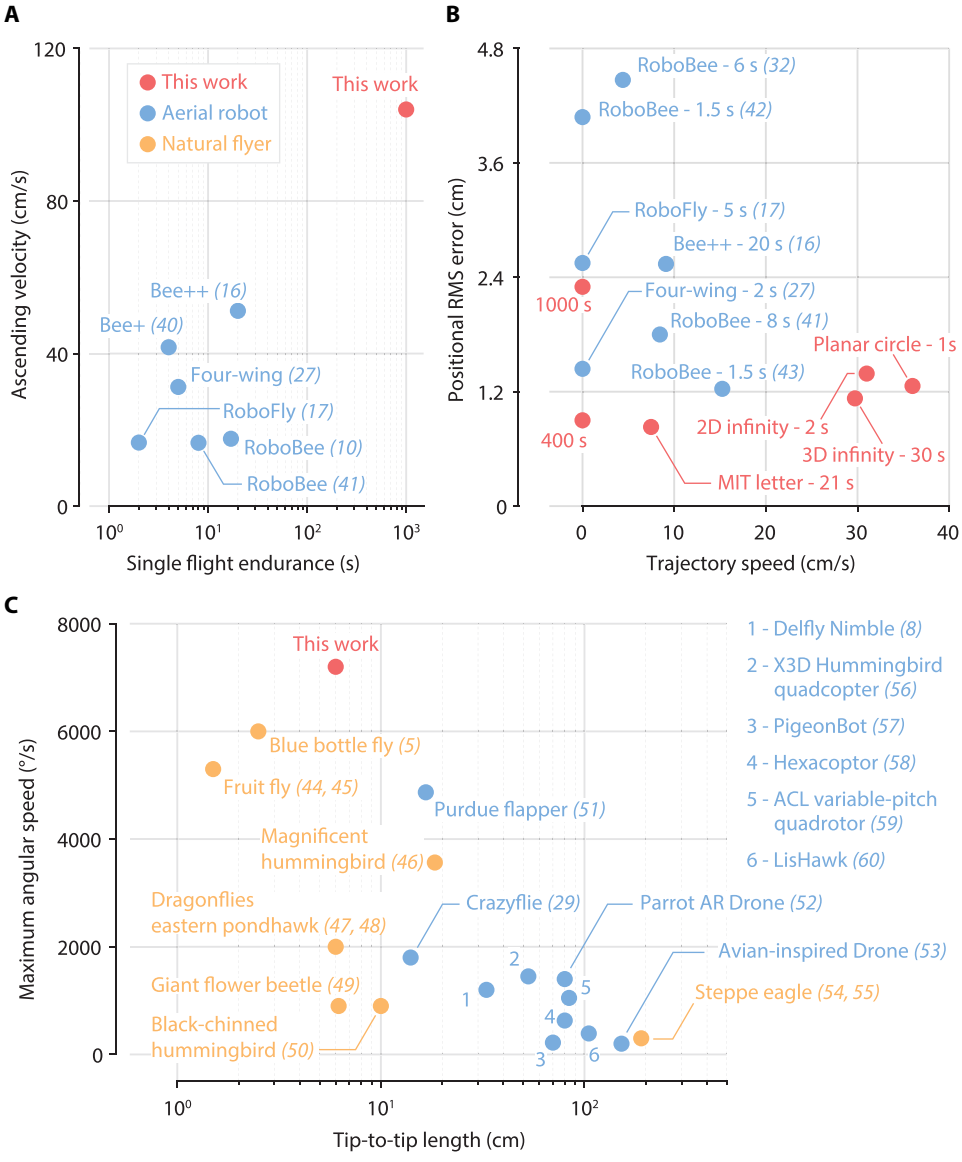

Fig. 7. Comparison of MAV flight performance. (**A**) Flight time and maximum ascending speed of existing subgram MAVs. (**B**) MAV mean flight speed and RMS position error during trajectory-following flight. (**C**) Maximum angular rotational rate as a function of vehicle length scale. The blue and orange dots represent MAV and insect performances, respectively (*40*–*60*).

Despite showing a large improvement in flight endurance, our robot lifetime remains two to three orders of magnitude shorter than that of mesoscale aerial robots, limiting potential applications. The robot has three failure modes: transmission softening, wing hinge tearing, and DEA degradation. In our prior works, wing hinge and transmission failure were the major limiting factor (80,000 flapping-wing cycles) given that the DEAs only experienced a 2% performance reduction after 2 million cycles of operation (*30*). In this work, we redesigned the transmission and wing hinge to reduce the flexural stress, which substantially improved the hinge and transmission endurance. We have not observed hinge or transmission failure in this work. However, the reduction in the transmission ratio led to higher actuation strain and required higher driving voltage. Compared with our prior work (*30*), the robot hovering voltage increased from 1500 to 1720 V. This high operating voltage caused 7.56% DEA degradation during the 330,000 cycles of operation, implying that the robot lifetime was limited by the actuator. There are two directions for further improving the robot lifetime. In the short term, the robot design could be adjusted to balance transmission and DEA degradation. Compared with the present work, the transmission ratio could be moderately increased to reduce actuation strain and improve system endurance. We estimate that a system-level redesign could lead to a two to five times improvement in flight time. In the longer term, lifetime improvement will be driven by new materials and processes. From the perspective of flexural materials,

future works may incorporate nitinol (*35*) and polymer (*36*) hinges in the SCM system because these materials have shown a high fatigue limit. From the perspective of DEA fabrication, other electrode materials such as graphene and silver nanowire may be explored because they have higher conductivity and produce less heat.

This robot platform has the potential to enable follow-up studies on control, sensing, and power autonomy (*37*). Although this work did not demonstrate heading angle control, it could be achieved by tilting each robot module during assembly (*16*, *38*). Owing to its consistency and long lifespan, this robot can be used to evaluate other planning frameworks, such as model predicative control or reinforcement learning. These planning methods can enable aggressive maneuvers such as banked turns and perching. More broadly, this robot is a fitting platform for exploring sensing and power autonomy, some of the most challenging directions for insect-scale MAVs. This robot has more than 500 mg of payload capacity, which is sufficient for carrying a sensor suite including gyroscopes, accelerometers, and small cameras. There still exists a moderate gap for this robot to achieve power autonomy. The DEA consumes 2.9 W of reactive power ($^1/_2CV^2f$) during hovering flight, where C is the total DEA capacitance, V is the applied voltage, and f is the flapping-wing frequency. At this scale, it is difficult for subgram circuits and batteries to deliver the required power and voltage. Toward enabling power autonomous flight, future studies should focus on improving robot aerodynamic efficiency and payload capacity.

MATERIALS AND METHODS

Fabrication of robot components

The robot airframe, transmissions, connecting bars, and wings were made through the SCM process. The airframe was made of 160 μm of carbon fiber, which consisted of orthogonally stacked M55J laminates. The airframe had 12 parts that were hand assembled into one structure (fig. S1A). This design had six I-beams for reinforcing structural strength and reducing oscillation during actuation.

The robot wing and wing hinge were combined into a single structure (Fig. 1C). There were seven material layers in the laminate fabrication process (fig. S1B). The top five layers consisted of carbon fiber (70 μm), adhesive (12 μm), polyimide (25 μm), adhesive (12 μm), and carbon fiber (70 μm), which functioned as the compliant flexure. The bottom two layers consisted of adhesive (12 μm) and polyester (1.5 μm), which acted as the wing. By combining the wing and wing hinge into one structure, this design removed the prior mating feature (*21*) and improved the component alignment and consistency. Compared with prior designs (Fig. 3A), the wing shape was adjusted to accommodate the long hinge along the wing leading edge, and the wing area was increased by two times. The wingspan (R), aspect ratio (AR), and first ($\hat{r}_1$) and second radius moments ($\hat{r}_2$) were 1.4 cm, 3, 0.49, and 0.55, respectively. On the basis of a blade element quasisteady model (*39*), the distance between the wing root and the wing spanwise COP was given as follows

$$R_{\text{cop}} = R\frac{\hat{r}_2^2}{\hat{r}_1} = 8.68 \text{ mm} \quad (1)$$

The robot transmission consisted of three sets of linear four-bar mechanisms. The central transmission (fig. S1C) had a width and length of 0.8 and 1.8 mm, respectively. Compared with prior works (*30*), the transmission stiffness increased by 50% and the transmission ratio decreased by 52%. These changes in transmission design aimed to increase the system resonance frequency and reduce the wing stroke amplitude. To mitigate off-axis bending, two guide transmissions were placed orthogonal to the main transmission (fig. S1C). The transmission stiffness of the guide transmissions was approximately 10% that of the main transmission, which implies that they have a small influence on system resonance and operating conditions.

The DEA was made using an existing fabrication method (*30*). We redesigned the DEA geometry to accommodate the transmission and wing design. Compared with the prior designs (*21*, *30*), the DEA length was reduced from 9 to 5 mm, and the number of electrode layers increased from 6 to 10. The electrode layer consisted of a single-wall carbon nanotube (Invisicon 3500, Nano-C Inc.) that was less than 30 nm thick. The elastomeric layer thickness was 36 μm, which was identical to that in a prior work (*30*). In this work, the DEA weighed 110 mg, and it is shown in fig. S1D. Compared with prior designs, this DEA showed an approximately two times increase in resonance frequency and blocked force, but it had a two times reduction in displacement. This design was advantageous because its short geometry mitigated nonlinear buckling (*21*). The robot was driven by four independent DEAs, each requiring a high-voltage line and a ground line. We designed two connector plates (fig. S1E) for the DEAs that shared the same ground line. This central connector plate design reduced the number of wires and mitigated wire-induced torques during flight. The "Selection of robot design parameters" section of Supplementary Methods describes the selection process of the robot design parameters, which is documented in table S1.

Experimental setup for static characterization and flight experiments

We conducted static and free flight experiments to characterize robot performance. In this work, we set up static flapping, constrained liftoff, constrained rotation, and free flight experiments. Figure S2A shows an image of the static flapping setup. The robot was affixed in front of a high-speed camera (Phantom VEO 710), and it was illuminated by a halogen light (Amscope HL150-A). A custom control computer (Speedgoat) sent the command signal into a high-voltage amplifier (Trek 677B), which drove the DEA in the range of 200 to 500 Hz and 1200 to 2000 V. The flapping-wing motion was recorded at 22,000 frames per second (fps). The recorded high-speed videos were processed manually to extract instantaneous flapping-wing kinematics (Fig. 2D). To extract the stroke amplitudes for multiple experiments (Fig. 2E), we modified an automated tracking method on the basis of a prior work (*21*).

After conducting the static flapping experiments, we drove the robot again under the same operating conditions while mounting it on a liftoff stand (fig. S2B). The liftoff stand consisted of a beam that was balanced around a pivot. If the robot generated higher force than its weight, it ascended upward. To precisely measure the average lift force, we placed different payloads on either side of the balance beam under different operating conditions. The liftoff process was recorded by the high-speed camera at 3000 fps, and then the liftoff angle was extracted through an automated algorithm (*28*). The net lift force was calculated on the basis of the tracked beam angle. The set of liftoff tests determined the optimal operating frequency and the voltage to force mapping in free flight experiments.

In preparation for body flip demonstrations, we conducted constrained rotation experiments (Fig. 2C). Figure S2C shows an image of the setup where one robot module was mounted around a beam.

To accurately estimate robot rotational speed in free flight experiments, the distance from the robot module to the rotation center was set to half of the robot connector length (Fig. 1B). The rotation center was approximately at the same location as the robot COM during free flight. We operated the robot at 1800 V and 330 Hz (movie S1 part 3 and Fig. 3C), and we recorded the high-speed video at 3000 fps. We manually tracked the beam angle (fig. S2I) and found the maximum rotational speed and average acceleration to be 9700° s^{-1} and 46,200° s^{-2}, respectively. This experiment demonstrated that our robot can generate a large body torque and achieve a large rotational speed.

We conducted a sequence of hovering (Fig. 4 and fig. S3), trajectory-tracking (Fig. 5 and figs. S4 to S7), and body flip (Fig. 6 and fig. S8 to S10) experiments to demonstrate robot flight capabilities. The experiments were performed in an existing flight arena (*30*) (fig. S3A). The flight arena was equipped with a motion capture system, custom Simulink-Realtime control hardware, and high-voltage amplifiers. In addition to using the same high-speed camera in previous parts, we also used a color camera (Sony FX3) for recording flight (fig. S3A). To ensure continuous tracking during the fast body flips, seven 1.5-mm reflective markers were mounted on both sides of the robot to improve tracking robustness. Five markers were placed on the robot's upward facing side, and two markers were placed on the bottom side. These seven markers had a net weight of 40 mg, which was 10% of the estimated net payload. The motion capture system returned tracked position and orientation data. To calculate velocity and rotational speed, we processed the data with a low-pass filter before taking numerical derivatives. The controller ran at 2 kHz and commanded the amplifiers at 10 kHz. The robot had four independently controlled DEAs, and it was tethered to the amplifiers through 49-gauge quadruple-insulated wires.

Statistical analysis

The boxplots in Fig. 5 (L and M) illustrate the position error distribution of four trajectory patterns ($N = 5$ for the 2D infinity, planar circle, and 3D infinity patterns, and $N = 6$ for the MIT pattern). The boxes show 25, 50, and 75 percentiles, and the black bars show minimum and maximum position errors. The data values are presented in table S2.

Supplementary Materials

The PDF file includes:

Methods
Figs. S1 to S10
Tables S1 and S2
Legends for movies S1 to S10
References (*61*, *62*)

Other Supplementary Material for this manuscript includes the following:

Movies S1 to S10

REFERENCES AND NOTES

1. G. Card, M. H. Dickinson, Visually mediated motor planning in the escape response of *Drosophila*. *Curr. Biol.* **18**, 1300–1307 (2008).
2. Z. J. Wang, J. Melfi Jr., A. Leonardo, Recovery mechanisms in the dragonfly righting reflex. *Science* **376**, 754–758 (2022).
3. P. Henningsson, L. C. Johansson, Downstroke and upstroke conflict during banked turns in butterflies. *J. R. Soc. Interface* **18**, 20210779 (2021).
4. J. A. Bender, M. H. Dickinson, Visual stimulation of saccades in magnetically tethered *Drosophila*. *J. Exp. Biol.* **209**, 3170–3182 (2006).
5. P. Liu, S. P. Sane, J.-M. Mongeau, J. Zhao, B. Cheng, Flies land upside down on a ceiling using rapid visually mediated rotational maneuvers. *Sci. Adv.* **5**, eaax1877 (2019).
6. J. M. Melis, I. Siwanowicz, M. H. Dickinson, Machine learning reveals the control mechanics of the insect wing hinge. bioRxiv 547116 [Preprint] (2023). https://doi.org/10.1101/2023.06.29.547116.
7. W. Salem, B. Cellini, H. Kabutz, H. K. Hari Prasad, B. Cheng, K. Jayaram, J.-M. Mongeau, Flies trade off stability and performance via adaptive compensation to wing damage. *Sci. Adv.* **8**, eabo0719 (2022).
8. M. Karásek, F. T. Muijres, C. De Wagter, B. D. W. Remes, G. C. H. E. de Croon, A tailless aerial robotic flapper reveals that flies use torque coupling in rapid banked turns. *Science* **361**, 1089–1094 (2018).
9. Z. Tu, F. Fei, J. Zhang, X. Deng, An at-scale tailless flapping-wing hummingbird robot. I. Design, optimization, and experimental validation. *IEEE Trans. Robot.* **36**, 1511–1525 (2020).
10. K. Y. Ma, P. Chirarattananon, S. B. Fuller, R. J. Wood, Controlled flight of a biologically inspired, insect-scale robot. *Science* **340**, 603–607 (2013).
11. L. Hines, D. Campolo, M. Sitti, Liftoff of a motor-driven, flapping-wing microaerial vehicle capable of resonance. *IEEE Trans. Robot.* **30**, 220–232 (2014).
12. D. S. Drew, N. O. Lambert, C. B. Schindler, K. S. J. Pister, Toward controlled flight of the ionocraft: A flying microrobot using electrohydrodynamic thrust with onboard sensing and no moving parts. *IEEE Robot. Autom. Lett.* **3**, 2807–2813 (2018).
13. H. V. Phan, H. C. Park, Mechanisms of collision recovery in flying beetles and flapping-wing robots. *Science* **370**, 1214–1219 (2020).
14. Y.-W. Chin, J. M. Kok, Y.-Q. Zhu, W.-L. Chan, J. S. Chahl, B. C. Khoo, G.-K. Lau, Efficient flapping wing drone arrests high-speed flight using post-stall soaring. *Sci. Robot.* **5**, eaba2386 (2020).
15. R. J. Wood, E. Steltz, R. S. Fearing, Optimal energy density piezoelectric bending actuators. *Sens. Actuators A Phys.* **119**, 476–488 (2005).
16. R. M. Bena, X. Yang, A. A. Calderón, N. O. Pérez-Arancibia, High-performance six-DOF flight control of the Bee^{++}: An inclined-stroke-plane approach. *IEEE Trans. Robot.* **39**, 1668–1684 (2023).
17. Y. M. Chukewad, J. James, A. Singh, S. Fuller, RoboFly: An insect-sized robot with simplified fabrication that is capable of flight, ground, and water surface locomotion. *IEEE Trans. Robot.* **37**, 2025–2040 (2021).
18. T. Ozaki, N. Ohta, T. Jimbo, K. Hamaguchi, A wireless radiofrequency-powered insect-scale flapping-wing aerial vehicle. *Nat. Electron.* **4**, 845–852 (2021).
19. M. A. Graule, P. Chirarattananon, S. B. Fuller, N. T. Jafferis, K. Y. Ma, M. Spenko, R. Kornbluh, R. J. Wood, Perching and takeoff of a robotic insect on overhangs using switchable electrostatic adhesion. *Science* **352**, 978–982 (2016).
20. Y. Chen, H. Wang, E. F. Helbling, N. T. Jafferis, R. Zufferey, A. Ong, K. Ma, N. Gravish, P. Chirarattananon, M. Kovac, R. J. Wood, A biologically inspired, flapping-wing, hybrid aerial-aquatic microrobot. *Sci. Robot.* **2**, eaao5619 (2017).
21. Y. Chen, H. Zhao, J. Mao, P. Chirarattananon, E. F. Helbling, N.-S. P. Hyun, D. R. Clarke, R. J. Wood, Controlled flight of a microrobot powered by soft artificial muscles. *Nature* **575**, 324–329 (2019).
22. S. Kim, Y.-H. Hsiao, Y. Lee, W. Zhu, Z. Ren, F. Niroui, Y. Chen, Laser-assisted failure recovery for dielectric elastomer actuators in aerial robots. *Sci. Robot.* **8**, eadf4278 (2023).
23. Y.-H. Hsiao, S. Kim, S. Ceron, Z. Ren, Y. Chen, Modular and scalable fabrication of insect-scale aerial robots toward demonstrating swarm flights. *Adv. Intell. Syst.* **6**, 2300059 (2024).
24. J. P. Whitney, P. S. Sreetharan, K. Y. Ma, R. J. Wood, Pop-up book MEMS. *J. Micromech. Microeng.* **21**, 115021 (2011).
25. E. Appel, J. Michels, S. N. Gorb, Resilin in insect flight systems. *Adv. Funct. Mater.* **34**, 2215162 (2024).
26. O. Kraft, R. Schwaiger, P. Wellner, Fatigue in thin films: Lifetime and damage formation. *Mater. Sci. Eng. A* **319-321**, 919–923 (2001).
27. S. B. Fuller, Four wings: An insect-sized aerial robot with steering ability and payload capacity for autonomy. *IEEE Robot. Autom. Lett.* **4**, 570–577 (2019).
28. Y. Chen, S. Xu, Z. Ren, P. Chirarattananon, Collision resilient insect-scale soft-actuated aerial robots with high agility. *IEEE Trans. Robot.* **37**, 1752–1764 (2021).
29. Y. Chen, N. O. Pérez-Arancibia, Controller synthesis and performance optimization for aerobatic quadrotor flight. *IEEE Trans. Control Syst. Technol.* **28**, 2204–2219 (2020).
30. Z. Ren, S. Kim, X. Ji, W. Zhu, F. Niroui, J. Kong, Y. Chen, A high-lift micro-aerial-robot powered by low-voltage and long-endurance dielectric elastomer actuators. *Adv. Mater.* **34**, 2106757 (2022).
31. Y. Chen, K. Ma, R. J. Wood, Influence of wing morphological and inertial parameters on flapping flight performance, in *2016 IEEE/RSJ International Conference on Intelligent Robots and Systems (IROS)* (IEEE, 2016), pp. 2329–2336.
32. R. McGill, N.-S. P. Hyun, R. J. Wood, Modeling and control of flapping-wing micro-aerial vehicles with harmonic sinusoids. *IEEE Robot. Autom. Lett.* **7**, 746–753 (2022).
33. P. Sareh, P. Chermprayong, M. Emmanuelli, H. Nadeem, M. Kovac, Rotorigami: A rotary origami protective system for robotic rotorcraft. *Sci. Robot.* **3**, eaah5228 (2018).

34. T. Helps, C. Romero, M. Taghavi, A. T. Conn, J. Rossiter, Liquid-amplified zipping actuators for micro-air vehicles with transmission-free flapping. *Sci. Robot.* **7**, eabi8189 (2022).
35. R. A. York, R. J. Wood, Nitinol living hinges for millimeter-sized robots and medical devices, in *International Conference on Robotics and Automation* (IEEE, 2019), pp. 889–893.
36. M. H. Rosen, G. Le Pivain, R. Sahai, N. T. Jafferis, R. J. Wood, Development of a 3.2 g untethered flapping-wing platform for flight energetics and control experiments, in *IEEE International Conference on Robotics and Automation* (IEEE, 2016), pp. 3227–3233.
37. E. F. Helbling, R. J. Wood, A review of propulsion, power, and control architectures for insect-scale flapping-wing vehicles. *Appl. Mech. Rev.* **70**, 010801 (2018).
38. Y.-H. Hsiao, S. Kim, Z. Ren, Y. Chen, Heading control of a long-endurance insect-scale aerial robot powered by soft artificial muscles, in *2023 IEEE International Conference on Robotics and Automation (ICRA)* (IEEE, 2023), pp. 3376–3382.
39. J. P. Whitney, R. J. Wood, Aeromechanics of passive rotation in flapping flight. *J. Fluid Mech.* **660**, 197–220 (2010).
40. X. Yang, Y. Chen, L. Chang, A. A. Calderon, N. O. Perez-Arancibia, Bee$^+$: A 95-mg four-winged insect-scale flying robot driven by twinned unimorph actuators. *IEEE Robot. Autom. Lett.* **4**, 4270–4277 (2019).
41. P. Chirarattananon, K. Y. Ma, R. J. Wood, Adaptive control of a millimeter-scale flapping-wing robot. *Bioinspir. Biomim.* **9**, 025004 (2014).
42. A. De, R. McGill, R. J. Wood, An efficient, modular controller for flapping flight composing model-based and model-free components. *Int. J. Robot. Res.* **41**, 441–457 (2022).
43. P. Chirarattananon, K. Y. Ma, R. J. Wood, Single-loop control and trajectory following of a flapping-wing microrobot, in *2014 IEEE International Conference on Robotics and Automation (ICRA)* (IEEE, 2014), pp. 37–44.
44. F. T. Muijres, M. J. Elzinga, J. M. Melis, M. H. Dickinson, Flies evade looming targets by executing rapid visually directed banked turns. *Science* **344**, 172–177 (2014).
45. A. Susanto, S. Sudarjat, E. Yulia, A. D. Permana, A. Gunawan, D. H. Yudistira, Effectiveness of modified traps for protection against fruit flies on mango. *J. Biodjati* **5**, 99–106 (2020).
46. B. Cheng, B. W. Tobalske, D. R. Powers, T. L. Hedrick, Y. Wang, S. M. Wethington, G. T.-C. Chiu, X. Deng, Flight mechanics and control of escape manoeuvres in hummingbirds. II. Aerodynamic force production, flight control and performance limitations. *J. Exp. Biol.* **219**, 3532–3543 (2016).
47. S. Zeyghami, H. Dong, Study of turning takeoff maneuver in free-flying dragonflies: Effect of dynamic coupling. arXiv:1502.06858 [physics.flu-dyn] (2015).
48. C. Li, H. Dong, Wing kinematics measurement and aerodynamics of a dragonfly in turning flight. *Bioinspir. Biomim.* **12**, 026001 (2017).
49. Y. Li, F. Cao, T. T. V. Doan, H. Sato, Controlled banked turns in coleopteran flight measured by a miniature wireless inertial measurement unit. *Bioinspir. Biomim.* **11**, 056018 (2016).
50. W. H. Baltosser, S. M. Russell, Black-chinned hummingbird (*Archilochus alexandri*), version 2.0, in *The Birds of North America*, A. F. Poole, F. B. Gill, Eds. (Cornell Lab of Ornithology, 2000).
51. Z. Tu, F. Fei, X. Deng, Bio-inspired rapid escape and tight body flip on an at-scale flapping wing hummingbird robot via reinforcement learning. *IEEE Trans. Robot.* **37**, 1742–1751 (2021).
52. F. Oliva-Palomo, A. Sanchez-Orta, P. Castillo, H. Alazki, Nonlinear ellipsoid based attitude control for aggressive trajectories in a quadrotor: Closed-loop multi-flips implementation. *Control Eng. Pract.* **77**, 150–161 (2018).
53. E. Ajanic, M. Feroskhan, V. Wüest, D. Floreano, Sharp turning maneuvers with avian-inspired wing and tail morphing. *Commun. Eng.* **1**, 34 (2022).
54. G. Taylor, M. Bacic, A. Carruthers, J. Gillies, Y. Ozawa, A. Thomas, Flight control mechanisms in birds of prey, in *45th AIAA Aerospace Sciences Meeting and Exhibit* (AIAA, 2007), pp. 39.
55. B.-U. Meyburg, P. Paillat, C. Meyburg, Migration routes of Steppe eagles between Asia and Africa: A study by means of satellite telemetry. *Condor* **105**, 219–227 (2003).
56. S. Lupashin, A. Schöllig, M. Sherback, R. D'Andrea, A simple learning strategy for high-speed quadrocopter multi-flips, in *2010 IEEE International Conference on Robotics and Automation* (IEEE, 2010), pp. 1642–1648.
57. E. Chang, L. Y. Matloff, A. K. Stowers, D. Lentink, Soft biohybrid morphing wings with feathers underactuated by wrist and finger motion. *Sci. Robot.* **5**, eaay1246 (2020).
58. A. Tagliabue, J. P. How, Efficient deep learning of robust policies from MPC using imitation and tube-guided data augmentation. arXiv:2306.00286 [cs.RO] (2023).
59. M. Cutler, J. P. How, Analysis and control of a variable-pitch quadrotor for agile flight. *J. Dyn. Syst. Meas. Control* **137**, 101002 (2015).
60. E. Ajanic, M. Feroskhan, S. Mintchev, F. Noca, D. Floreano, Bioinspired wing and tail morphing extends drone flight capabilities. *Sci. Robot.* **5**, eabc2897 (2020).
61. H. Zhao, A. M. Hussain, M. Duduta, D. M. Vogt, R. J. Wood, D. R. Clarke, Compact dielectric elastomer linear actuators. *Adv. Funct. Mater.* **28**, 1804328 (2018).
62. Y. Chen, N. Gravish, A. L. Desbiens, R. Malka, R. J. Wood, Experimental and computational studies of the aerodynamic performance of a flapping and passively rotating insect wing. *J. Fluid Mech.* **791**, 1–33 (2016).

Acknowledgments: We thank Q. Kieu for discussion and help with image processing. **Funding:** This work was supported by the National Science Foundation grants 2202477 and 2236708 (Y.C.) and Mathworks Fellowship (Y.-H.H.). **Author contributions:** Conceptualization: S.K., Y.-H.H., and Y.C. Methodology: S.K., Y.-H.H., and Y.C. Software: Y.-H.H., S.K., Z.R., J.H., and Y.C. Validation: Y.-H.H., S.K., Z.R., J.H., and Y.C. Formal analysis: Y.-H.H., S.K., Z.R., J.H., and Y.C. Investigation: S.K., Y.H., and Y.C. Resources: Y.C. Data curation: S.K., Y.-H.H., and Y.C. Writing–original draft: S.K., Y.-H.H., and Y.C. Writing–review and editing: Y.-H.H., S.K., Z.R., J.H., and Y.C. Visualization: Y.-H.H., S.K., Z.R., J.H., and Y.C. Supervision: Y.C. Project administration: Y.C. Funding acquisition: Y.C. **Competing interests:** The authors declare that they have no competing interests. **Data and materials availability:** The flight data are available in the data repository Dryad with the following DOI: https://doi.org/10.5061/dryad.0p2ngf28q.

Submitted 25 March 2024
Accepted 10 December 2024
Published 15 January 2025
10.1126/scirobotics.adp4256